Effects of different bionic strengthening technologies on fatigue crack growth behavior of AZ31B magnesium alloy TIG-welded joints

Yong-heng JIANG[1#], Xin-lei QIU[1#], Zheng-qiang ZHANG[1],
Zi-heng SONG[2], Sheng-guang DAI[1], Xue-lei WANG[1], Chun WU[1], Chao MENG[1]

1. College of Materials Science and Engineering, Liaoning Technical University, Fuxin 123000, China;
2. Key Laboratory of Electromagnetic Processing of Materials (Ministry of Education),
Northeastern University, Shenyang 110819, China

Abstract: With the aim of improving the fatigue properties of Mg alloy welded joints under cyclic loading, the effects of laser bionic treatment and ultrasonic impact bionic treatment on the fatigue crack growth (FCG) behavior of AZ31B Mg alloy TIG-welded joints were studied and compared. The results show that bionic treatment refines the grains on the joint surface and improves the microhardness. In the crack stable growth stage, both bionic samples exhibit a lower FCG rate and a higher FCG resistance. The two bionic treatment methods reduce the probability of crack initiation and partially promote crack deflection, providing a new approach for improving the FCG behavior of welded joints.
Key words: magnesium alloy; laser bionic treatment; ultrasonic impact bionic treatment; microstructure; fatigue crack growth

1 Introduction

Magnesium (Mg) alloys, as the lightest metal-based structural materials, exhibit high specific strengths and specific stiffness, and have significant potential to replace steel and aluminum alloys, especially considering that their lightweight nature can promote an increased energy efficiency when used in vehicles [1−3]. Welding is commonly used to connect structural materials, with tungsten inert gas (TIG) welding being widely used for welding Mg alloys owing to its economic advantages, ease of use, and convenience [4]. However, the TIG welding process often leads to microstructural coarsening in the welded joints after cooling owing to the large heat input, which often weakens the welded joints during fatigue failure and limits the

application of welded Mg alloy components [5]. It is therefore desirable to improve the fatigue properties of such Mg alloy welded joints.

The fatigue strength and fatigue crack growth (FCG) behavior of materials determine their fatigue properties. To date, extensive research has been conducted to improve the fatigue strengths of Mg alloys and their welded joints [6−8]. However, few studies have focused on improving the FCG behavior of Mg alloys, particularly in the context of their welded joints. Thus, it is necessary to study the FCG behavior of Mg alloy welded joints to improve their FCG resistance characteristics. The FCG behavior of a component is closely related to its strength and toughness. Although an enhancement in strength can hinder the initiation of fatigue cracks and reduce the number of crack nucleation points, a higher toughness can extend

# Yong-heng JIANG and Xin-lei QIU contributed equally to this work
Corresponding author: Chao MENG, Tel: +86-18242858562, E-mail: mengchao_ja@yeah.net

the FCG path by consuming the FCG energy. Consequently, the synergistic effect between the strength and toughness properties can be employed to significantly improve the fatigue properties of materials [9,10]. However, the majority of related research carried out to date has focused on homogeneous materials, with research into heterogeneous materials (such as Mg alloy welded joints) being limited. The feasibility of realizing synergistic strengthening to improve the FCG behavior of Mg alloy welded joints using surface treatment technologies should therefore be investigated. However, the general trade-off between strength and toughness presents challenges in terms of achieving good strength−toughness combinations in a single material. Therefore, understanding the relationship between strength and toughness is of great significance for studying the FCG behavior of materials.

To break this deadlock, the natural "soft−hard" alternating structure could provide a novel design approach, wherein the soft phase exhibits a good toughness and absorbs a large amount of deformation, while the hard phase has a high strength and hinders crack initiation [11]. This natural alternating structure transcends most engineering materials, providing good strength−toughness combinations, and so it can be considered suitable for application as a bionic prototype to improve the fatigue properties of components. Laser surface remelting (LSR) is a widely recognized surface-processing method suitable for use in bionic treatment owing to its rapid heating and cooling characteristics. In this context, WANG et al [12] used LSR technology to prepare bionic samples with alternating distributions of soft (untreated) and hard (laser-treated) zones on the surface of S355 low carbon steel, significantly improving the strength and plasticity due to the stress redistribution and grain refinement. In another study, SHI et al [13] prepared a stripe-like bionic structure on the surface of an AZ31B Mg alloy TIG-welded joint by laser remelting, resulting in a significant deflection of the FCG path of the bionic sample, and reducing the effective stress intensity factor range (ΔK_{eff}) and FCG rate to improve the FCG resistance of the bionic sample. It was therefore apparent that the construction of a bionic structure by laser bionic

treatment (LBT) on the metal surface achieves a good strength−toughness combination to improve the FCG behavior.

Ultrasonic impact treatment (UIT) is an effective technology for improving the fatigue properties of welded joints. It can significantly reduce the degree of stress concentration in welded joints and reconfigure the stress field by introducing compressive residual stress (CRS), which is beneficial for improving the FCG behavior of welded joints [14,15]. In addition, the output energy of UIT is concentrated, and the processing area is controllable, allowing the generation of an impact hardening area of a certain size on the component surface [16,17]. Due to the ease of realizing the alternating soft−hard structure using the UIT technology, it would be desirable to investigate the FCG behavior of welded joints with bionic structures introduced by UIT. It is expected that the combination of UIT and bionic strengthening will provide new approaches for improving the FCG behavior of welded joints.

Thus, in the current study, alternating soft and hard bionic structures are prepared on TIG-welded joints of the AZ31B Mg alloy using LSR and UIT, respectively. The changes in the microstructure, microhardness, FCG behavior, and fatigue fracture characteristics of the AZ31B Mg alloy TIG-welded joints enabled by LSR and UIT are compared and analyzed. Moreover, the strengthening mechanisms for improving the FCG behavior of the welded joints processed by the two methods are revealed.

2 Experimental

2.1 Materials

The hot-rolled AZ31B Mg alloy plates with dimensions of 300 mm (rolling direction, RD) × 100 mm (transverse direction, TD) × 10 mm (normal direction, ND) were used. The chemical compositions of the hot-rolled AZ31B Mg alloy plates are listed in Table 1. Welding wire diameter was 2 mm, which cut from the AZ31B Mg alloy plates.

Table 1 Chemical compositions of AZ31B Mg alloy (wt.%)

Al	Zn	Mn	Si	Cu	Fe	Mg
2.5−3.5	0.7−1.3	0.2	0.3	0.05	0.005	Bal.

2.2 Sample preparation

Prior to welding, the surfaces of the welding wire and the AZ31B Mg alloy plate (double 'V' groove type) were polished with sandpaper to remove the oxide film formed on the surface. The surfaces were then cleaned using alcohol. Double-sided TIG welding was then carried out (see Fig. 1(a)), wherein the welding direction was consistent with the RD. The welding parameters included a welding current of 190 A, a welding voltage of 22.6 V, a welding speed of 2.5 mm/s, and Ar (99.90% in purity) as the shielding gas. Prior to bionic treatment, the weld reinforcement was removed using sandpaper, and the surface was cleaned with alcohol. Based on the bionic prototype (Fig. 1(b)), a double-sided symmetrical bionic structure (Fig. 1(c)) was prepared on the welded joint using a pulsed Nd^{3+}:YAG laser (laser power of 1900 W, spot diameter of 2.5 mm, scan speed of 20 mm/s, and bionic fringe spacing of 6 mm). The laser-treated welded joint zone was denoted as WLZ, while the laser-treated base metal (BM) zone was denoted as BLZ. UIT was carried out using a UIT−125 instrument. The bionic prototype was identical to that used for LBT, and the bionic fringe spacing was 6 mm (Fig. 1(d)). The UIT processing parameters were as follows: impact current of 1.6 A, and impact speed of 40 mm/min. The applied pressure corresponded to the weight of the ultrasonic impact equipment. The welded joint zone subjected to UIT was denoted as WUZ, while the untreated welded joint was denoted as UWJ. The compact tensile (CT) samples used for the fatigue crack growth tests were cut using wire electrical discharge machining (EDM), as shown in Figs. 1(c₁, d₁). For all CT samples, the axial loading stress was parallel to the bionic treatment stripe, and perpendicular to the RD direction.

2.3 Properties test

Microhardness measurements were performed using a rotary microhardness tester (HV−1000Z, China) with a load of 0.1 kg and a hold time of 10 s. The final hardness value was reported as the average of three measurements. A nanoindentation instrument (Anton Paar NHT2, Austria) was used to measure the residual stress on the material surface after the UIT. Fatigue crack growth experiments were performed according to the international standard ASTM E647─2015. Sinusoidal waveform cyclic loading and tensile stress loading modes were adopted. The stress ratio ($R=P_{min}/P_{max}$), wherein P_{min} and P_{max} are the minimum and maximum loads, respectively, was equal to 0.1, while the loading frequency was 10 Hz. By gradually reducing the load, a fatigue pre-crack of 2.5 mm was extended from the notch root of the CT sample. After the pre-crack was successfully fabricated, the test was continued under a constant stress amplitude. The crack length was calculated from the datum plane and measured using the flexibility method according to national standard GB/T 6389─2017. During the test, the crack length was indirectly calculated using the crack opening
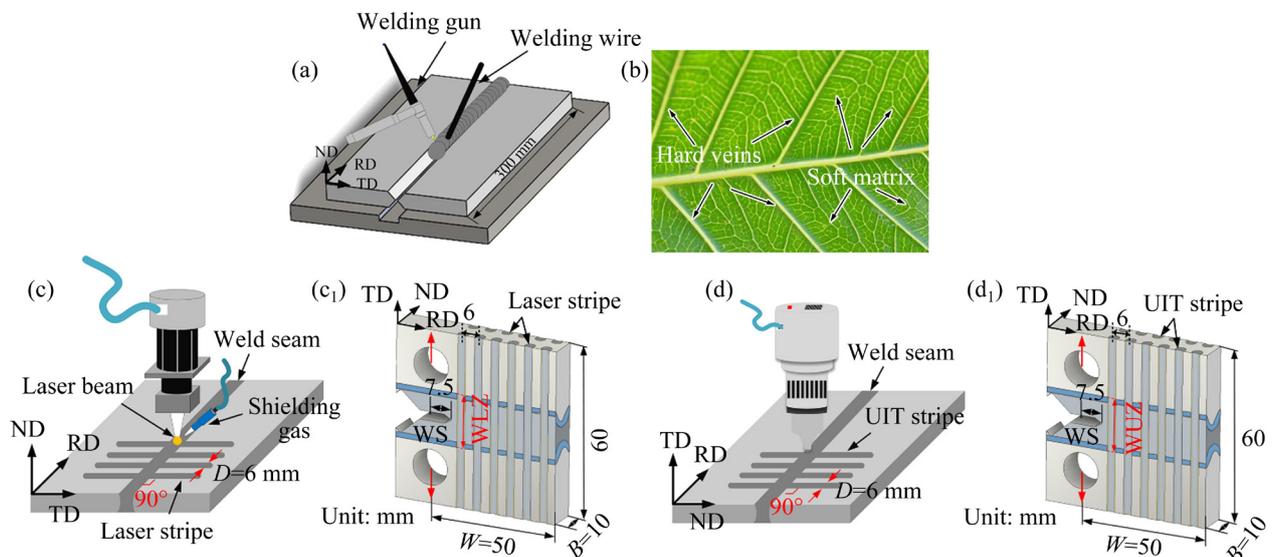

Fig. 1 Structural diagrams of TIG welding process (a), bionic prototype (b), LBT process (c), LBT bionic sample with notch in WS (c₁), UIT process (d), and UIT bionic sample with notch in WS (d₁)

displacement monitored in real-time using an MTS 623.03 F-20. The relationship between the flexibility and the crack length is expressed using the dimensionless flexibility (M):

$$M = \frac{BE\Delta\mu}{P} \tag{1}$$

where E is the Young's modulus, B is the thickness of the sample, P is the applied load, and $\Delta\mu$ is the crack opening displacement at the crack opening.

The crack length, a, of the sample can be calculated based on its flexibility as follows:

$$\frac{a}{W} = C_0 + C_1 U_x + C_2 U_x^2 + C_3 U_x^3 + C_4 U_x^4 + C_5 U_x^5 \tag{2}$$

$$U_x = \frac{1}{\sqrt{M}+1} \tag{3}$$

where a/W is the normalized crack size (a is the crack length, W is the sample width) and C_i is the regression coefficient, which is determined by the measurement position of the normalized flexibility. In addition, $C_0 = 1.0002$, $C_1 = -4.0632$, $C_2 = 11.242$, $C_3 = -106.04$, $C_4 = 464.33$, and $C_5 = -650.68$.

In addition, the stress intensity factor range (ΔK) is calculated as follows:

$$\Delta K = \frac{\Delta P}{B\sqrt{W}}\frac{(2+\alpha)}{(1-\alpha)^{3/2}} \cdot$$
$$\left(0.886 + 4.64\alpha - 13.32\alpha^2 + 14.72\alpha^3 - 5.6\alpha^4\right) \tag{4}$$

where ΔP is the applied load range, and $\alpha = a/W$. The ΔK value corresponding to a $\mathrm{d}a/\mathrm{d}N$ value of 10^{-7} mm/r (N is the cycle number) was defined as FCG threshold (ΔK_{th}). According to the standard, the frequency and stress ratio were maintained constant with the pre-crack stage, and the ΔK_{th} was determined according to the ΔK-decreasing test. More specifically, for each 10% decrease in ΔK, the crack length increased by 0.2 mm. The test was terminated when the value of $\mathrm{d}a/\mathrm{d}N$ approached 10^{-7} mm/r. The 10 data pairs with the lowest FCG rate were selected, and the linear regression method was used to fit and solve the $\lg(\mathrm{d}a/\mathrm{d}N) - \lg \Delta K$ coordinate system to give ΔK_{th}.

The curve of $\mathrm{d}a/\mathrm{d}N - \Delta K$ was plotted in a logarithmic coordinate system, and fatigue cracks in the medium growth rate range underwent a stable growth process following the standard Paris formula:

$$\frac{\mathrm{d}a}{\mathrm{d}N} = C(\Delta K)^m \tag{5}$$

where C is the material constant, and m is the Paris index, which represents the fitting slope of the $\mathrm{d}a/\mathrm{d}N - \Delta K$ curve in the logarithmic coordinates. When $\mathrm{d}a/\mathrm{d}N$ exceeds 10^{-2} mm/r, it increased rapidly, and the curve tended to be parallel to the y-axis. Therefore, the ΔK value corresponding to 10^{-2} mm/r was defined as the critical stress intensity factor range (ΔK_{cr}) [18]. When the ΔK value exceeded ΔK_{cr}, the FCG process passed from the stable growth stage to the high-speed instability stage.

2.4 Microstructure analysis

The polished samples were etched using an oxalic acid nitric acid solution (1 g oxalic acid + 49 mL distilled water + 1 mL nitric acid). Laser confocal scanning microscopy (LEXT OLS4000, Japan) was used to observe the microstructure and the FCG path. Electron backscatter diffraction (EBSD) experiments were carried out using a sample that had been mechanically polished and placed in a 10 vol.% perchlorate methanol solution for 20 s at 30 V. The EBSD test was performed using a scanning electron microscope (SEM, Zeiss Merlin Compact, Germany) equipped with accessories (Oxford, Nordlys Nano, UK) at an inclination angle of 70°, an acceleration voltage of 20 kV, and a working distance of 13−14 mm. HKL Channel 5 software was used to analyze the microstructure, crystal orientation, and Schmid factor (SF) distribution in each specified region. SEM (JSM−7500F, Japan) was used to observe the fatigue fracture characteristics, while high-resolution transmission electron microscopy (TEM, FEI Talos F200X G2, USA) was used to observe the microstructure of the UIBT sample surface.

3 Results

3.1 Microstructure

3.1.1 LBT sample

Figure 2 shows microstructural characteristics of the LBT sample cross-section, wherein it can be seen that the microstructural characteristics of the different regions differ significantly owing to the effects of the heat inputs associated with TIG welding and laser treatment (Fig. 2(a)). As shown in Figs. 2(b, c), the BM is mainly composed of unevenly sized equiaxed grains and a few twins,
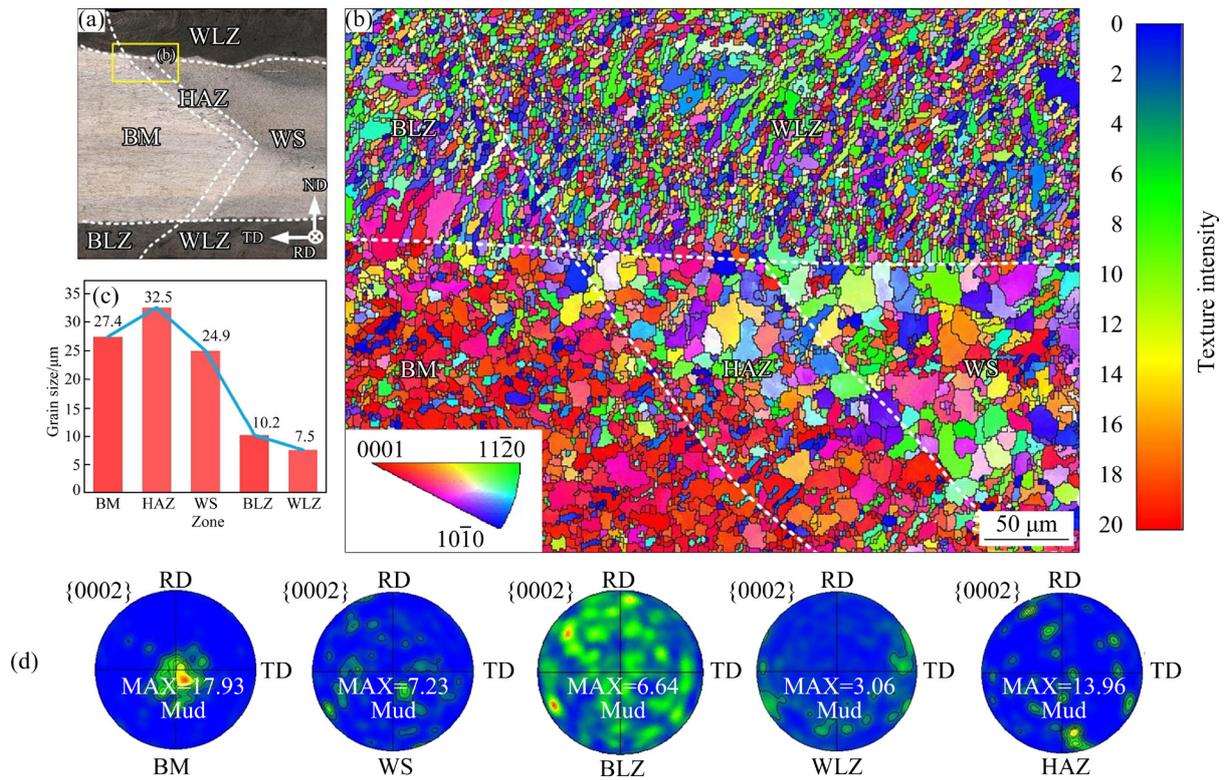
Fig. 2 Cross-sectional morphology (a), inverse pole figure (IPF) (b), average grain sizes (c) and pole figures (d) of different zones of LBT sample

wherein the average grain size is 27.4 μm. The average grain size of the heat affected zone (HAZ) is increased to 32.5 μm, and the average grain size of the weld seam (WS) is 24.9 μm. The average grain size of the BLZ is 10.2 μm, and the characteristics typical of epitaxial growth are observed. The equiaxed and columnar grains are uniformly distributed in the WLZ, and the average grain size of the WLZ is 7.5 μm. Figure 2(d) shows the pole figures obtained for the different regions, wherein it is apparent that the BM possesses a strong {0002} basal texture. Owing to the small temperature gradient during TIG welding, no preferential crystal growth is observed in the WS [19], resulting in a random grain orientation in the WS, thereby accounting for the weak textural intensity at the weld. In contrast, the HAZ exhibits a higher textural intensity than the WS, and deviates from the {0002} basal texture. This can be attributed to the fact that the HAZ close to the BM possesses a large temperature gradient, which results in selective growth of grains. The grains in the WLZ are equiaxed without a preferred orientation, and the textural intensity is low. However, the textural intensity of the grains in the

BLZ is greater than that in the WLZ owing to epitaxial growth.

3.1.2 UIT sample

An impact deforming layer with a depth of ~1871 μm is formed on the surface of the WS after UIT, and the grain size of the WUZ is found to be finer than that of the WS (Fig. 3(a)). With an increase in depth, the energy input by UIT gradually decreases until it disappears; thus, the grain refinement effect of the WUZ gradually weakens (Fig. 3(b)). The color of inverse pole figure in the WUZ tends to be red, indicating a preferred orientation of the grains in the WUZ, which is verified in the pole figure, forming the (0002) basal texture. In addition, since some degree of residual stress exists on the sample surface following UIT, a number of grains on the top surface are not displayed because of the low resolution. Figure 3(c) shows the band contrast (BC) map corresponding to the IPF given in Fig. 3(b). The grayscale range from dark to light (from top to bottom) indicates that the degree of deformation gradually weakens. Thus, the region with the largest deformation is located at the top of the WUZ. This can be attributed to the fact that a larger deformation energy induces the
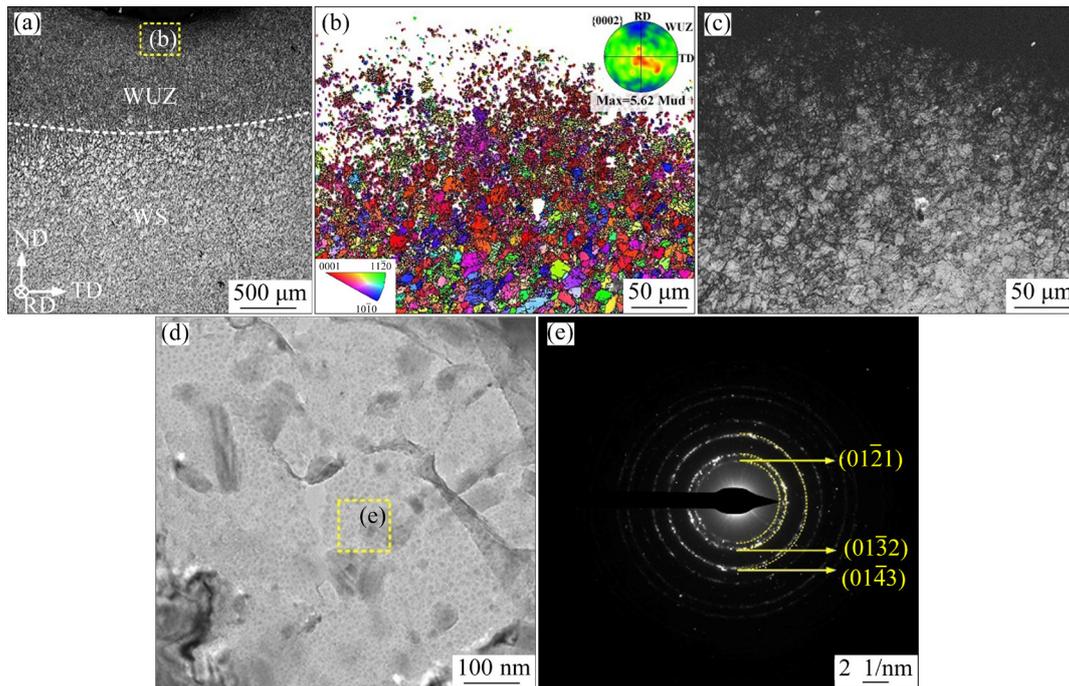
Fig. 3 Macrograph of UIT cross-section (a), inverse pole figure (b) of area indicated by yellow box in (a), BC map of WUZ (c), TEM image of top layer of UIT sample (d), and SAED pattern (e) for yellow region indicated in (d)

recrystallization of the grains and a dense nano-crystalline layer is formed. To more accurately analyze the microstructure of the top region of the WUZ, TEM was employed. As shown in Fig. 3(d), nanoparticles with an average grain size of ~20 nm appear in the top region of the WUZ. In addition, the selected-area electron diffraction (SAED) pattern is approximately circular, indicating the presence of a large number of randomly distributed ultrafine grains, as shown in Fig. 3(e).

3.2 Microhardness

The hardness test results for the LBT and UIT samples are shown in Fig. 4, wherein it can be seen that the maximum hardness value of the laser treated zone reaches $HV_{0.1}$ 68.7, which is 19.5% higher than that of WS. This is attributed to rapid heating and cooling that occur during laser processing, which refines the grains of the WLZ. Following UIT, fine nanograins and high-density dislocations are generated on the WUZ surface, with a peak microhardness value of $HV_{0.1}$ 102.2 being recorded. The interactions among the dislocations divides the original grains to achieve refinement, which is accompanied by a strong work-hardening effect, significantly increasing the microhardness. However, the hardness value
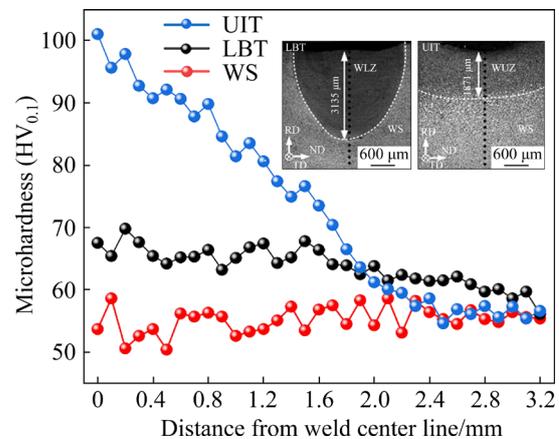

Fig. 4 Microhardness for cross-sections of bionic samples obtained using different treatment methods

gradually decreases with an increasing depth from the surface, eventually approaching the hardness value of the WS ($HV_{0.1}$ 57.5).

3.3 FCG behavior

3.3.1 FCG characteristics of different stages

In general, the FCG rate curve can be divided into three stages, namely the low-rate crack growth stage, the stable crack growth stage (medium-rate stage), and the crack instability growth stage (high-rate stage). Figure 5(a) summarizes the ΔK_{th} values obtained for the different samples. After
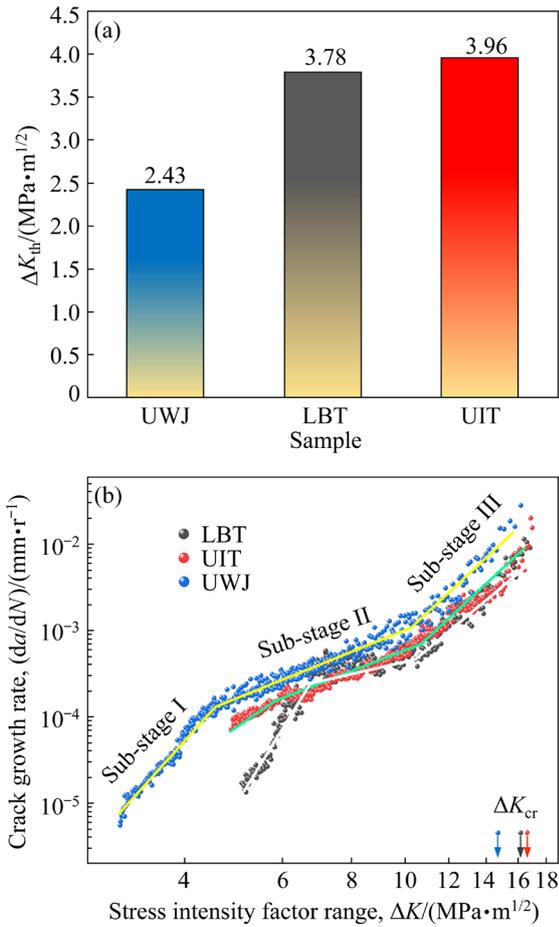
Fig. 5 ΔK_{th} values (a) and $da/dN-\Delta K$ curves (b) of different samples

bionic treatment, the ΔK_{th} values of the LBT and UIT samples increase to 3.78 and 3.96 MPa·m$^{1/2}$, respectively, which are 55.56% and 62.96% higher than that of UWJ sample. These results indicate that both bionic treatment methods improve the crack growth resistance of the WS. However, owing to the higher strength and hardness of the nanograins on the UIBT sample surface, the fatigue crack threshold is larger, and the initiation and growth of prefabricated cracks become more difficult.

Figure 5(b) shows the relationship between da/dN and ΔK for the different AZ31B Mg alloy joint samples. In general, for traditional materials, only one slope exists during stable crack growth; however, it is found that the different samples demonstrate obvious inflection points during crack stable growth, indicating the presence of three obvious sub-stages with three distinguishable Paris slopes. With an increase in ΔK, the curves gradually tend to converge. Notably, many studies have reported that deformed Mg alloys and their joints deviate from traditional single-stage crack stable growth at a stress ratio of 0.1, instead exhibiting three different sub-stages of crack stable growth. It is required that at low stress ratios, the FCG behavior represents an obvious sensitivity toward the microstructure, which often leads to the occurrence of transition points [12,20−24]. It is found that the FCG rate curves of the samples obtained using different treatment methods exhibit a common trend. More specifically, crack growth produces an S-shaped curve, wherein the three sub-stages of crack stable growth are apparent. Sub-stage I possesses a larger slope, while Sub-stage II has a gentle slope, indicating that the FCG rate increases slowly with an increase in the stress intensity factor. Furthermore, the slope of Sub-stage III increases rapidly, but remains smaller than that of Sub-stage I. In addition, the $da/dN-\Delta K$ fitting curves of both bionic samples lie below those of the UWJ sample, indicating that the UIT and LBT samples exhibit lower FCG rates at equivalent ΔK values. Notably, both treatment approaches improve the FCG behavior of the UWJ sample due to the fact that they change the original grain size and crystal orientation, thereby enhancing the FCG resistance [20]. Table 2 summarizes the Paris law constants and the ΔK values corresponding to the inflection points obtained using multiple fitting equations for the different samples.

Table 2 Summary of calculated Paris constants for different FCG rate results of different samples presented in Fig. 5

Sample	$(da/dN)/(mm·r^{-1})$			$\Delta K/(mPa·m^{1/2})$			
	Sub-stage I	Sub-stage II	Sub-stage III	ΔK_{TI}	ΔK_{TII}	ΔK_{cr}	ΔK_{fin}
UWJ	$1.69\times10^{-9}(\Delta K)^{7.54}$	$2.13\times10^{-6}(\Delta K)^{2.71}$	$1.46\times10^{-10}(\Delta K)^{6.72}$	4.37	10.76	14.84	16.19
LBT	$8.97\times10^{-12}(\Delta K)^{8.88}$	$3.37\times10^{-5}(\Delta K)^{1.18}$	$3.27\times10^{-10}(\Delta K)^{6.05}$	7.66	10.76	16.31	16.81
UIT	$4.51\times10^{-9}(\Delta K)^{6.04}$	$1.66\times10^{-6}(\Delta K)^{2.58}$	$6.66\times10^{-11}(\Delta K)^{6.73}$	5.81	11.98	16.88	16.41

ΔK_{TI} and ΔK_{TII} are the ΔK values corresponding to the turning points between Sub-stages I and II, and Sub-stages II and III, respectively; ΔK_{fin} is the corresponding ΔK value at the end of the test

To further compare the FCG behavior of the two bionic samples, their crack opening displacement (COD) were investigated, since the COD effectively reflects the FCG resistance of a material. The UIT sample exhibits the largest COD_{min} at relatively a low ΔK value ($\Delta K < 7$ MPa·m$^{1/2}$), indicating that the UIT sample exhibits a lower plastic deformation resistance and cracking resistance than the LBT sample under the same load conditions, resulting in easier crack growth. The lower COD_{min} of the LBT sample demonstrates a superior FCG resistance and crack-closure ability. With an increasing value of ΔK ($\Delta K > 10$ MPa·m$^{1/2}$), the $COD_{min}-\Delta K$ curves of both samples deflect, with the curve of the LBT sample being more obvious, and matching with the inflection point of the da/d$N-\Delta K$ curve. This further indicates that the FCG behavior is sensitive to the microstructure. In addition, with an increasing value of ΔK, the COD_{min} of the LBT sample increases rapidly, and gradually tends to be consistent with that of the UIT sample, indicating that the FCG resistance of LBT sample decreases under high ΔK conditions. This can be explained as follows: the large enough load becomes sufficient to act as the main factor determining the crack growth. Furthermore, the COD_{max} and COD_{min} values of the UIT sample are significantly higher than those of the LBT sample, indicating that the FCG resistance of the LBT sample is greater than that of UIT sample during the entire FCG process. This phenomenon is caused by the different treatment zone depths resulting from the two bionic treatment approaches. More specifically, the WLZ and WUZ depths are 3135 and 1871 μm, respectively, and based on these results, it is apparent that a shallower depth leads to limited improvement in FCG behavior. In Fig. 6(b), it can be seen that the da/d$N-\Delta K_{eff}$ curve distributions of the two samples are significantly different. Notably, ΔK_{eff} is the actual driving force that determines crack growth, thereby reflecting the FCG resistance of each sample. For low values of ΔK_{eff}, no significant differences are found in the FCG rates between the two samples, indicating similar crack growth resistances for the LBT and UIT samples during the initial crack growth stage. During the overall process, increasing FCG rate leads to gradual dispersion of the da/d$N-\Delta K_{eff}$ curves for both bionic samples due to the sensitivity of the FCG

behavior to the microstructure. The obvious grain refinement hinders fatigue crack growth, causing significant fluctuations in the crack growth rate, which is consistent with the results presented in Figs. 5(b) and 6(a). When the number of cycles is equal, the LBT sample possesses the largest ΔK_{eff}, requiring a greater driving force for rapid crack growth. With an increasing value of ΔK_{eff}, the da/d$N-\Delta K_{eff}$ curves of the LBT and UIBT samples gradually begin to overlap, thereby indicating similar crack growth resistances.
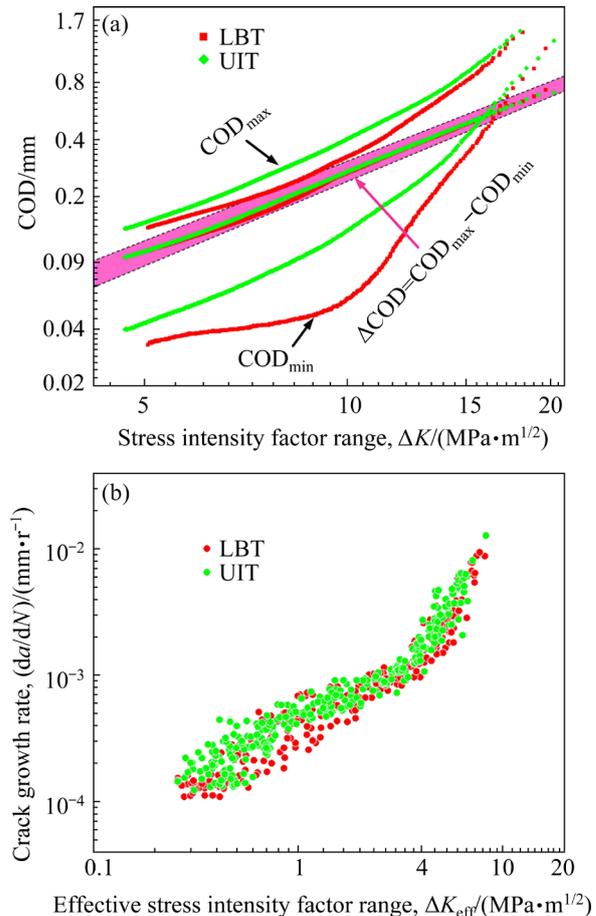

Fig. 6 COD$-\Delta K$ curves (a) and da/d$N-\Delta K_{eff}$ plots (b) for LBT and UIT samples

3.3.2 FCG path

As shown in Fig. 7(a), in the case of the LBT sample, the cracks are frequently deflected throughout the crack growth process. In addition, in the crack growth region (CGR), secondary cracks and twins can be seen to appear in the WS (Fig. 7(b)). Notably, the appearance and deflection of secondary cracks consume large amounts of energy and reduce ΔK_{eff} at the crack tip, thereby reducing the FCG rate. The appearance of twins increases the grain boundary density, hindering the

crack from propagating forward along the twin boundaries, and resulting in obvious crack deflection [25]. No obvious twins are found in the WLZ because the refined grains cannot effectively meet the energy conditions required for twin nucleation [25]. When the crack extends from the coarse-grained zone (WS zone) to the WLZ zone with finer grains, the crack tip becomes passivated and deflected (Fig. 7(c)), which improves the toughness of the material [26]. Roughness measurements along the sample surface reveal that the WLZ with a higher plastic deformation resistance exhibits a lower roughness, while the WS with a lower plastic deformation resistance possesses a higher roughness, as shown in Fig. 7(d). This is attributed to the FCG driving force and plastic deformation zone at the crack tip gradually increasing during crack growth, thereby resulting in a higher twin density and the occurrence of deformation in the WS. At this point, the presence of microcracks is also more obvious (Fig. 7(e)).

As shown in Fig. 8, the UIT and LBT samples display similar FCG path characteristics, wherein the macroscopic path of the FCG is Type I along the horizontal direction. Compared to the LBT sample, the UIT sample exhibits more frequent deflection, which is beneficial for generating effective crack closure and reducing the FCG rate (Fig. 8(a)). Notably, the macroscopic crack growth path of the UIT sample exhibits a small-angle deflection after the prefabricated crack. When the crack extends to the WUZ, owing to the ultrahigh hardness and highly refined grains present in the WUZ, this system is more able to resist plastic deformation, promoting an obvious deflection in the FCG direction. During the crack growth stage, the cracks in the WS are severely deflected, resulting in secondary cracks and twins (Figs. 8(b, c)). In the later stage of crack growth, severe plastic deformation occurs in the WS and additional microcracks appear (Fig. 8(d)). Furthermore, Fig. 8(e) shows the microstructural characteristics of the UIT sample close to the ΔK_{cr} value, wherein it can be seen that plastic deformation is more pronounced in the WS, and the surface becomes rougher. This is attributed to the fact that the impact affected zone undergoes obvious plastic deformation during the ultrasonic impact process,
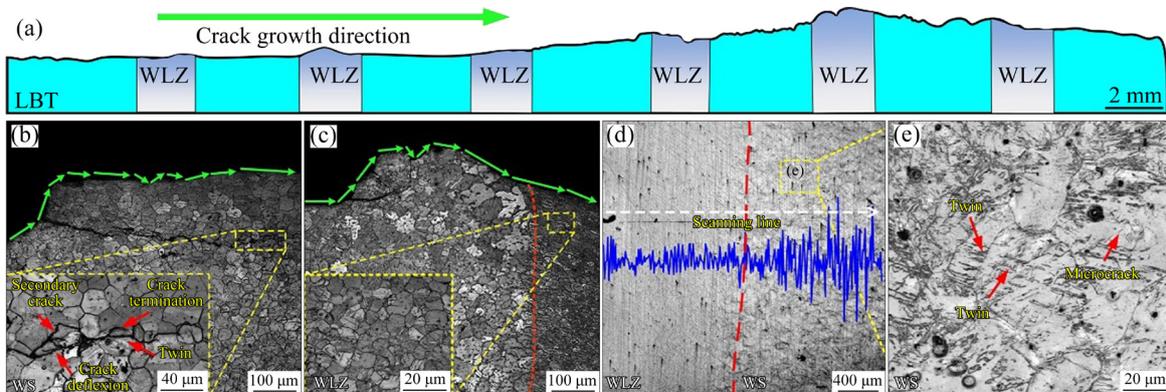

Fig. 7 FCG path for LBT sample (a), and microstructures of LBT sample at CGR (b, c) and ΔK_{cr} value (d, e)
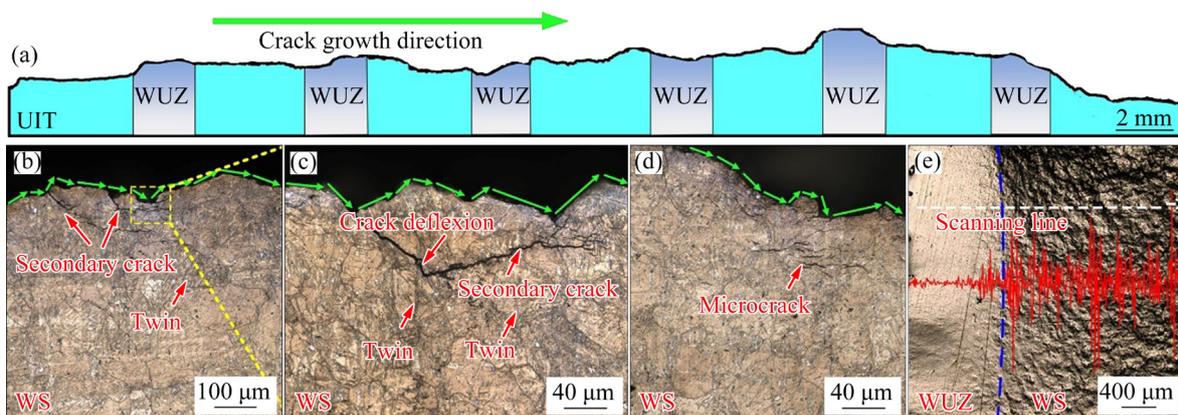

Fig. 8 FCG path for UIT sample (a), and microstructures of UIT sample at CGR (b, c) and ΔK_{cr} value (d, e)

forming high-density twins. Moreover, the microhardness also increases significantly during this process, resulting in an enhanced plastic deformation resistance.

3.3.3 Fatigue fracture analysis

Figure 9 shows the fatigue fracture characteristics of the different regions of the UWJ sample. As shown in Figs. 9(a, b), the fracture presents clear cleavage steps and river patterns in the CGR. In addition, secondary cracks, layered structures, and voids are observed on the fracture surface. Notably, similar layered structures have been observed in the fatigue fracture morphologies of other Mg alloys [27]. In the final fracture region (FFR), numerous elongated dimples and tearing ridges appear along the FCG direction, as shown in Fig. 9(c).
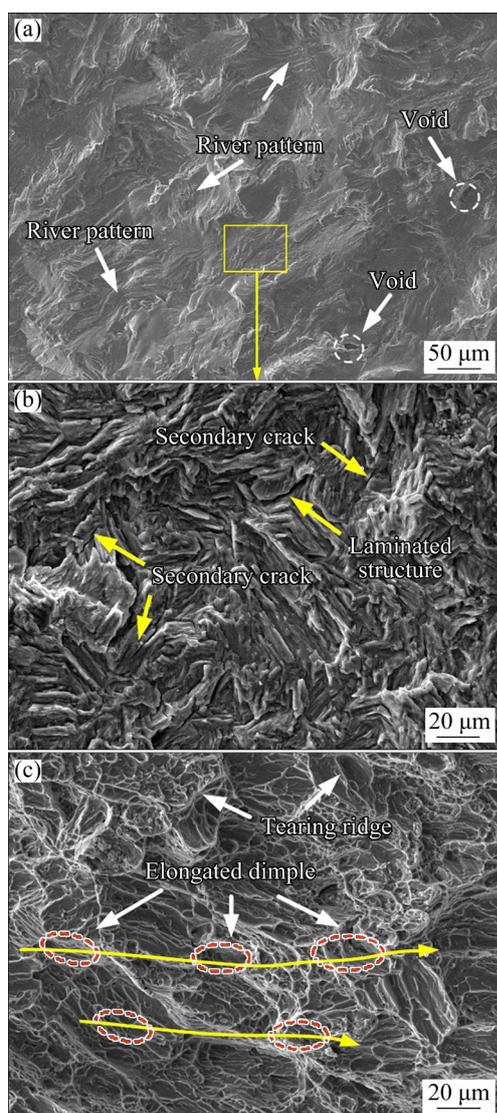

Fig. 9 Micrograph fracture characteristics for CGR (a, b) and FFR (c) of UWJ sample

Figure 10 shows the fatigue fracture characteristics of the different regions of the LBT sample, wherein it can be seen that the CGR and FFR exhibit significantly different macroscopic fracture characteristics (Fig. 10(a)). As shown in Figs. 10(b−e), the fracture characteristics of the CGR mainly include cleavage steps and river patterns, with an obvious transgranular cleavage fracture mode being apparent. In addition, the direction of the cleavage step is different. Furthermore, from Fig. 10(b), it can be seen that as the crack grows from the WS to the WLZ, the cleavage step decreases, the FCG direction is deflected, and the rough fracture becomes smooth due to grain refinement of the WLZ. Moreover, the LSR exhibits a fine grain structure with a random orientation, which leads to additional opportunities for the WLZ microcracks to deflect into grains with different orientations, resulting in smaller cleavage steps that run in different directions, along with a reduction in the FCG rate. The fracture surfaces of the WS and WLZ also possess typical secondary cracks (Fig. 10(c)), with a larger number of these secondary cracks being observed in the WLZ. This leads to greater energy consumption during crack growth, reduces the stress concentration at the crack tip, and lowers the FCG rate. Additionally, many fine equiaxed dimple edges are present in the WLZ, which exhibits obvious deformation (Fig. 10(d)). This indicates that the plastic deformation resistance is superior in this region, and that crack growth requires a greater amount of energy. Moreover, the directions of the dimples and tearing ridges in the WS are more diverse (Fig. 10(e)), indicating that the FCG direction changes significantly.

Figure 11 shows the fracture morphology of the UIT sample. It can be seen that in the CGR, a substantial number of river patterns emerge in the vicinity of the impact zone near the sample surface, and the orientation of the river pattern changes (Figs. 11(a, b)), indicating that the crack growth direction is deflected. In addition, unlike the fracture characteristics of the LBT sample, cleavage steps and secondary cracks are less pronounced in the UIT sample. This is attributed to the fact that UIT leads to significant grain refinement, forming a gradient structure and nanocrystals that effectively improve the plasticity of the material. In the FFR, the WUZ is found to possess highly concentrated
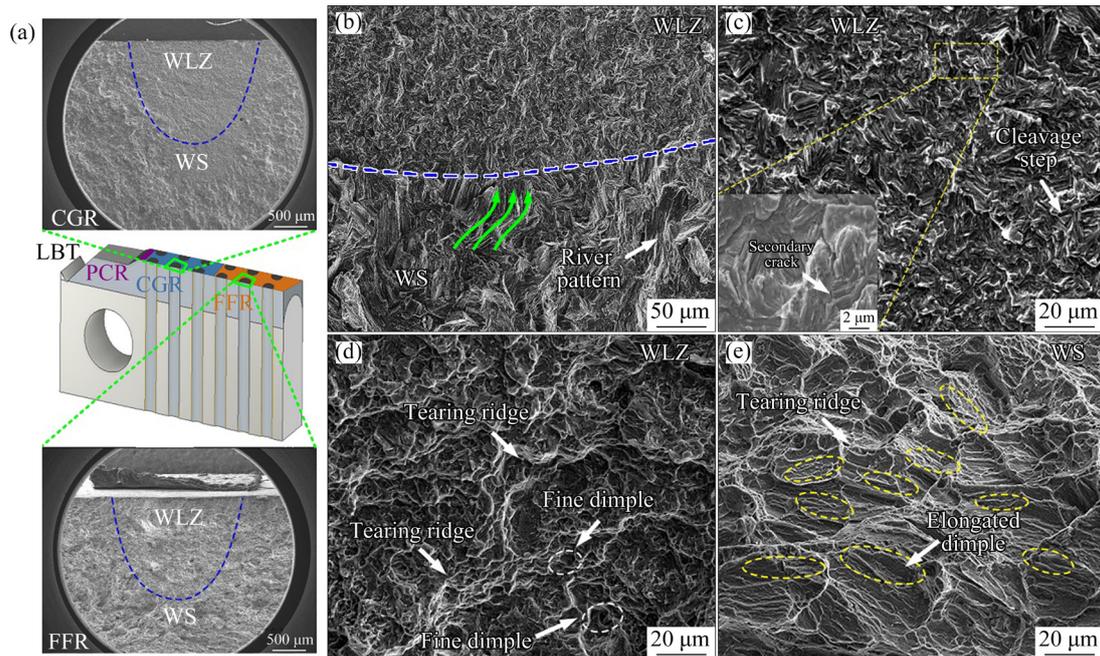
Fig. 10 Facture characteristics of LBT sample: (a) Macroscopic fatigue fracture; (b, c) At CGR; (d, e) At FFR
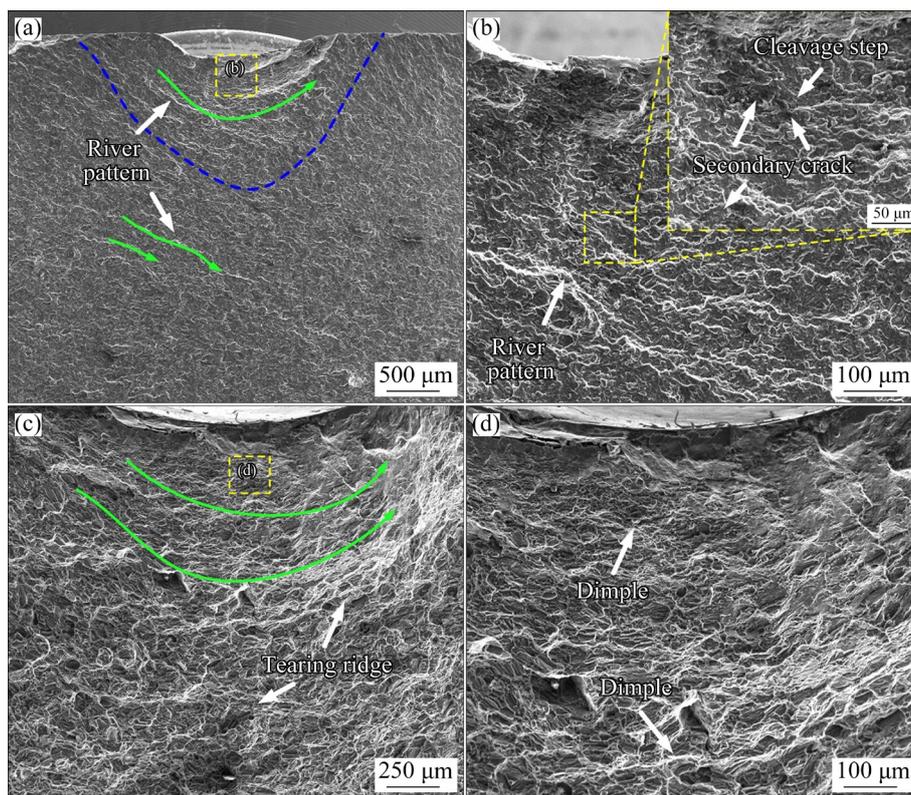

Fig. 11 Facture characteristics of UIT sample at CGR (a, b) and FFR (c, d)

small dimples and numerous evident tearing ridges (Figs. 11(c, d)). This change in the tearing ridge also reflects a change in the crack growth direction. Due to the severe plastic deformation induced by UIT, grain deformation and refinement occur, along with a change in the fatigue fracture pattern.

4 Discussion

4.1 Effect of microstructure on FCG behavior

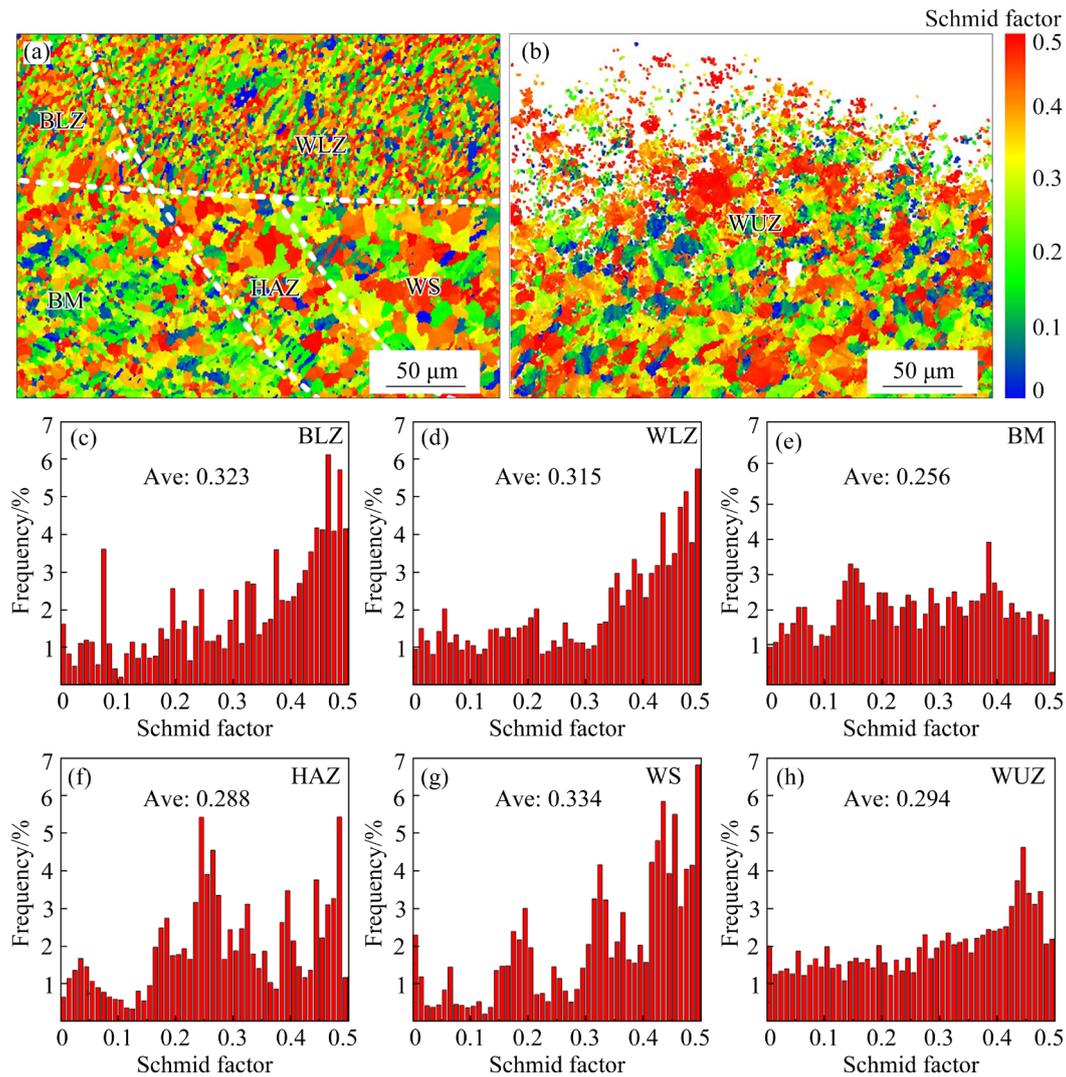Figure 12 shows the distribution of the SF for the $\{0001\}\langle11\bar{2}0\rangle$ basal plane slip systems in

Fig. 12 Schmid factor diagrams for LBT (a) and UIT (b) samples; Schmid factor distribution histograms for LBT (c−g) and UIT (h) samples

different regions of the LBT and UIT samples, wherein it is evident that the SF is lower in the BM and HAZ owing to the presence of a high textural intensity, as shown by the pole figure in Fig. 2(d). Therefore, the majority of grains show the "hard orientation". In addition, the grain distribution within the WS is found to be uniform, the grain size is relatively large, and the grain orientation is random. According to the Hall−Petch formula, the grain size is inversely proportional to the strength, and so the largest SF factor is obtained for the WS (Fig. 12(g)), easily meeting the critical shear stress required for slip band operation. Consequently, the resistance to plastic deformation is poor for this sample, resulting in a reduced strength. Following LBT, fine grains are detected in the WLZ and BLZ regions of the sample, and a fine grain

strengthening effect is induced, which leads to an increase in the strength of the treated zone and a decrease in the SF. This increase in strength inhibits crack initiation, thereby enhancing the overall FCG resistance. In addition, compared with the WLZ, the WUZ possesses ultrafine nanocrystals after UIT. As a result, the WUZ has a larger grain boundary volume fraction than the WLZ, and the SF of the WUZ is significantly lower than that of the WLZ (Fig. 12(h)). Therefore, in the fatigue crack initiation stage, the greater capability of UIBT to induce fine grain strengthening leads to the strain in the grain boundaries and grains within the WUZ being maintained at the same level, resulting in a more uniform stress distribution on the surface of the UIBT sample, thereby rendering surface crack initiation more difficult [28].

The kernel average misorientation (KAM) distributions of the LBT and UIT samples are shown in Figs. 13(a, b). The results show that the WUZ exhibits a high KAM value distribution, with higher KAM values being mainly distributed at the top of the WUZ. This indicates that severe plastic deformation occurs at the top of the WUZ. To explain the different effects of the two treatments on the FCG behavior of the sample in more detail, the geometrically necessary dislocation (GND) densities are determined for the different regions using following formula:

$$\rho^{GND} = \frac{2KAM_{ave}}{\mu b} = \frac{2\theta}{\mu b} \tag{6}$$

where θ is the local misorientation, μ represents the scan step size, and b is magnitude of the Burgers vector. The calculated GND densities are shown in Fig. 13(e), wherein it can be seen that the highest dislocation density is observed for the WUZ, followed by the WLZ, and then other regions. The high density of dislocations induces dislocation intersection and entanglement, leading to the "pinning effect" which hinders the dislocation movement and renders the initiation of slip systems more difficult. This impedes the plastic deformation of the material and increases its strength [29]. Consequently, the UIT sample is stronger than the LBT sample, which is consistent with SF results. This greater strength can effectively hinder the occurrence of deformation and improve the fatigue crack initiation resistance of materials [30]. Therefore, compared with the LBT sample, the UIBT sample is more effective in resisting crack initiation.
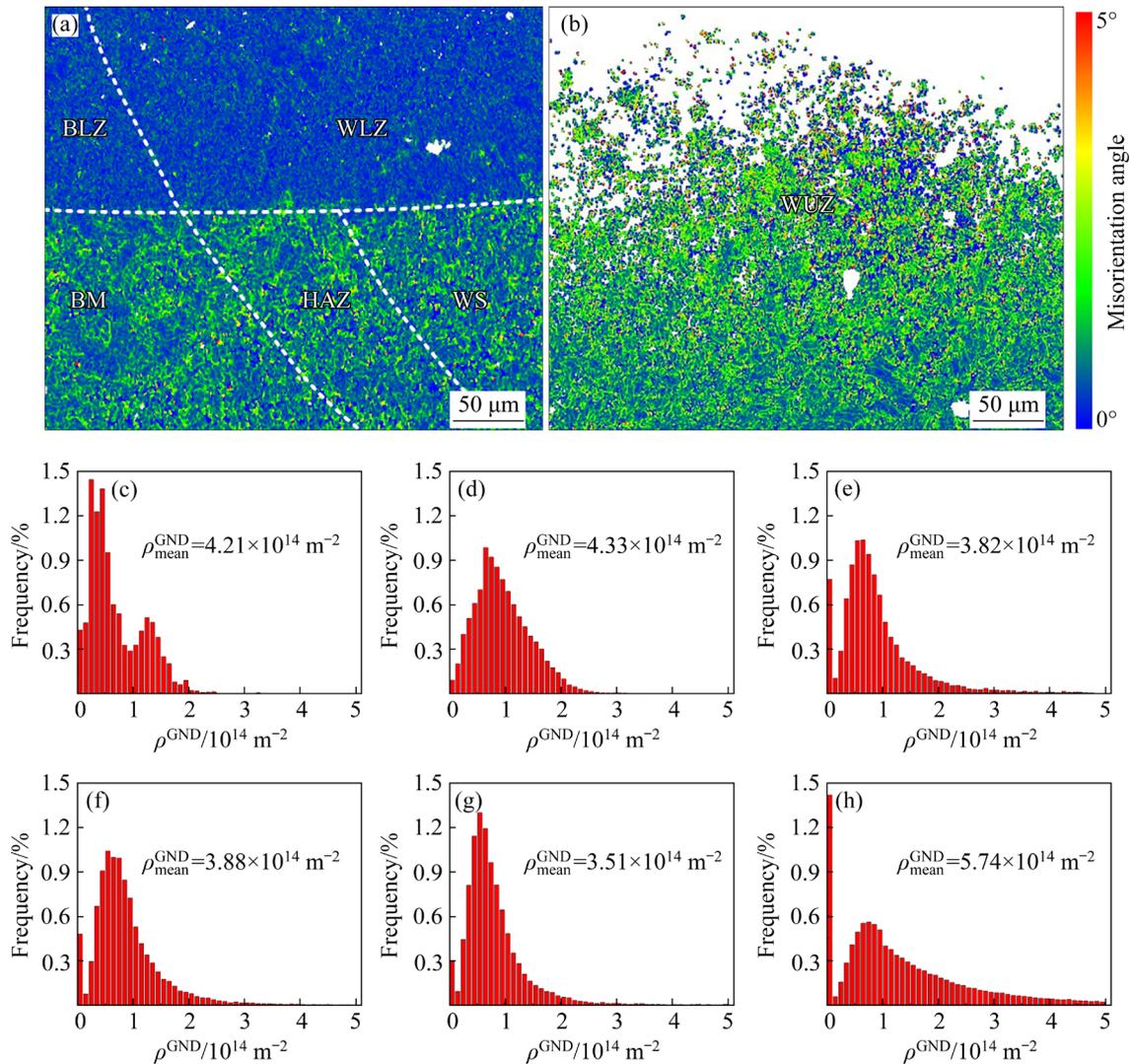

Fig. 13 KAM results for LBT (a) and UIT (b) samples; GND density distributions in BLZ (c), WLZ (d), BM (e), HAZ (f), WS (g), and WUZ (h)

The misorientation angle distributions in the different regions of the samples are presented in Fig. 14. A misorientation angle in the range of 2°−15° is defined as a low-angle grain boundary (LAGB), while misorientation angles >15° are defined as high-angle grain boundaries (HAGBs). It is found that LBT leads to an increase in the proportion of HAGBs in the WLZ (>90%). Importantly, these HAGBs inhibit crack growth, leading to crack deflection and branching. They can also increase the toughness of the material, which is beneficial in terms of delaying fatigue crack growth [7]. After UIT, the proportion of HAGBs clearly decreases in the WUZ, resulting in a lower toughness than that of the LBT sample. Therefore, compared with the UIT sample, during the crack growth stage, the LBT sample more effectively promotes the branching of fatigue cracks, thereby extending the fatigue crack growth path, consuming the energy required for crack growth, and reducing the fatigue crack growth rate.
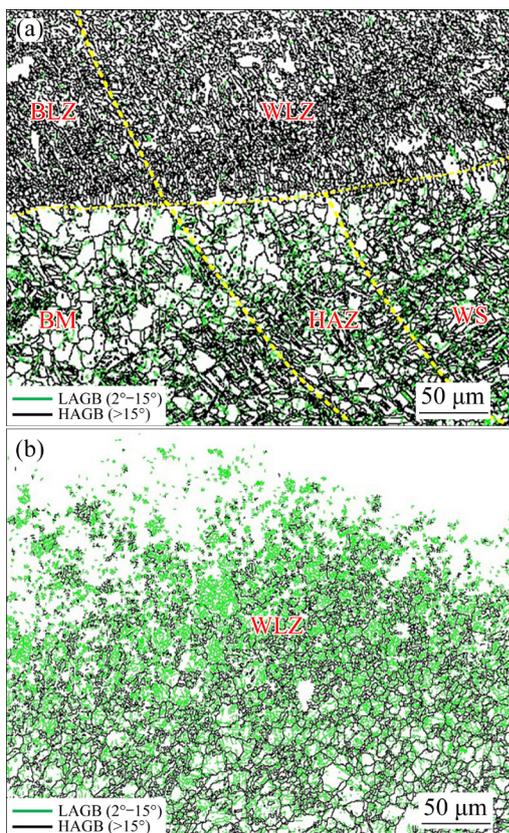

Fig. 14 Distribution of misorientation angles of LBT (a) and UIT (b) samples

However, it is found that the toughness of the UIT sample remains superior to that of the UWJ sample due to the "soft (WS)−hard (bionic treated zone)" alternating heterogeneous structure, which possesses different microstructures in the ND and RD directions of the material surface after the bionic treatment. When deformation occurs, a strain gradient is formed in the transition zone between the hard and soft zones to maintain the strain continuity, resulting in a large number of GNDs in transition zone. With the accumulation of GNDs, long-range stress occurs, which is known as heterogeneous induced deformation (HDI) stress [31,32]. Notably, HDI stress strengthening is a potential strengthening mechanism that increases the strength of heterogeneous materials. The strain hardening of HDI ensures that the material maintains a good plasticity [33]. In addition, the "soft and hard" combination of the WS and the bionic treated zone, and the large span grains size distribution, thereby allow the bionic hetero-structure to effectively develop HDI stress and realize synergistic improvements in the material strength and ductility [34,35]. Therefore, compared with the UWJ sample, both the LBT and UIT samples exhibit lower FCG rates and superior FCG resistance during the entire FCG stage.

4.2 Effect of residual stress on FCG behavior

LBT tailors the microstructure of a joint surface through the high-density heat input of the laser, whereas UIT is a cold deformation technology that treats the joint surface via severe plastic deformation. Therefore, due to these different processes, the types of residual stress introduced in the treatment zone differ. However, the direction of the residual stress remains parallel to the axial load of the FCG test since the processing direction is consistent with axial load. Owing to the large heat input and no deformation of the material, LBT produces a certain amount of residual tensile stress in the treatment zone. MENG et al [36] found that there was a certain amount of residual tensile stress in the LBT zone when using a laser bionic and ultrasonic impact composite technology to treat an AZ31B Mg alloy TIG-welded joint. Notably, the residual tensile stress supplements the energy lost during the stable crack growth process, thereby accelerating crack growth and reducing the FCG resistance. Therefore, in Sub-stage I of the da/d$N−$ ΔK curve (Fig. 5), the higher curve slope of the LBT sample indicates that it is sensitive to stress. Furthermore, a transformation is found to occur on

the sample surface in the stress state following UIT, and the residual tensile stress after welding is converted into residual compressive stress.

Nanoindentation is a nondestructive measurement technology that is primarily used for the measurement of residual stress. As shown in Fig. 15, which presents the nanoindentation curve of the UIT sample, when a load is applied, the indenter requires a greater amount of force to penetrate the top of the WUZ, and this requires force gradually decreasing with an increasing depth. During unloading, the maximum indentation depth (h_{max}) and the residual indentation depth (h_f) of the unimpacted weld zone are larger than those of the WUZ, indicating that the WUZ demonstrates a superior deformation resistance, as shown in Fig. 15(a). The elastic moduli of the top, middle, and bottom regions of the WUZ are 49.12, 46.24, and 45.81 GPa, respectively, while the elastic modulus of the WS is 42.34 GPa. Figure 15(b) shows the time−depth curve, including the loading, loading holding, and unloading stages. After the unloading stage, the welded joint exhibits elastic rebound and energy release. The residual stress values in different zones were calculated using the Suresh model [37]. Moreover, the residual tensile stress (Eq. (7)) and residual compressive stress (Eq. (8)) are calculated as follows:

$$\sigma = H\left(1 - \frac{h_0^2}{h^2}\right) \tag{7}$$

$$\sigma = \frac{H}{\sin \alpha'}\left(\frac{h_0^2}{h^2} - 1\right) \tag{8}$$

where H is the nano hardness of the material, α' is the angle between the pressure head and the surface deformation at 22°, h_0 is the indentation depth of the material without residual stress, and h is the indentation depth of the test material. Although a tensile residual stress of (148.4±10) MPa exists at the WS, this is transformed into compressive residual stress at the WUZ after UIT, giving a value of (−323.62±40) MPa at the top of the WUZ. Notably, a high CRS is important for improving the fatigue crack life and reducing the sensitivity of the fatigue crack gap. Previously, it has been reported that residual compressive stress fields can shift the initiation position of fatigue cracks from the material surface to the subsurface [38]. The existence of CRS inhibits local stress concentration,
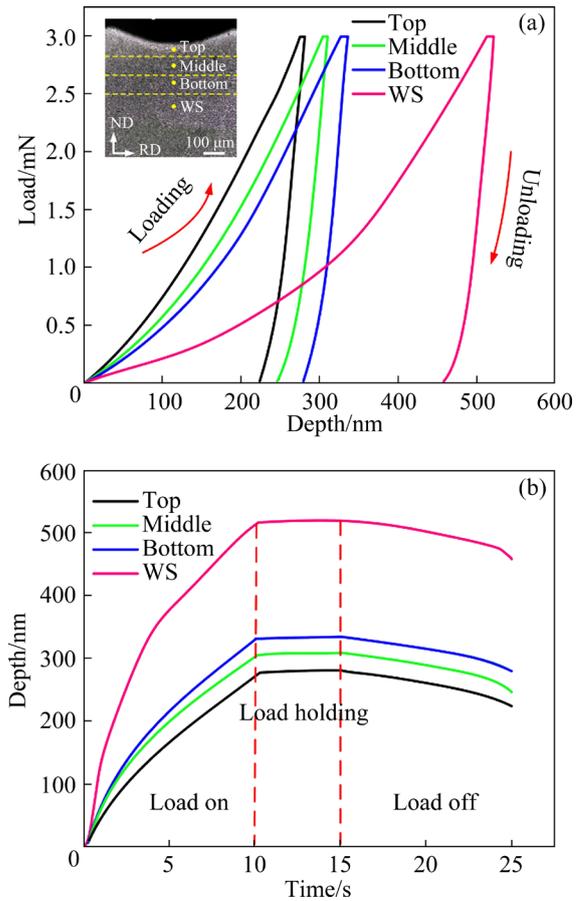

Fig. 15 Nanoindentation test results at different depths of WUZ: (a) Load−depth curves; (b) Depth−time curves

resulting in a decrease in the local load stress of fatigue crack initiation, which inhibits the initiation of surface cracks. In contrast, the CRS significantly affects the fatigue crack growth, balancing the partial tensile stress, reducing the fatigue crack growth rate, and enhancing the fatigue crack closure effect. The range of stress intensity factor (ΔK_{CRG}) and the range of effective stress intensity factor (ΔK_{eff}^{CRS}) in the presence of CRS can be expressed as follows:

$$\Delta K_{CRG} = K_{max} - K_{min} + K_{CRS} \tag{9}$$

$$\Delta K_{eff}^{CRS} = K_{max} - K_{op} + K_{CRS} \tag{10}$$

where K_{max} and K_{min} are the maximum and minimum values of the applied load, respectively, K_{CRS} is the residual stress, and K_{op} is the applied load when the crack is actually opened. When K_{CRS} refers to the compressive residual stress, ΔK_{CRG} and ΔK_{eff}^{CRS} decrease, leading to a reduction in the crack growth driving force and the effective stress intensity factor at the crack tip; ultimately, this

slows fatigue crack initiation and the subsequent crack growth rate [39]. The CRS formed during UIBT is gradually released during fatigue loading, resulting in a similar crack growth rate between the LBT and UIBT samples at Sub-stage III stage.

5 Conclusions

(1) LBT generates equiaxed grains with a random orientation on the joint surface. The grain size is 7.5 μm, and the microhardness is found to be ~19.5% higher than that of the WS. In contrast, UIT produces a hardened layer with a nano- crystalline structure and high-density dislocations at the top of the deformation layer; its microhardness is ~77.7% higher than that of WS.

(2) In the Sub-stage I, the slope obtained for the UIT sample is particularly low, while in Sub-stage II, the LBT sample exhibits the lowest FCG rate. Both LBT and UIT make the FCG path become tortuous, but the UIT sample is more obvious.

(3) LBT sample exhibits a river pattern, cleavage steps, and typical secondary cracks after fracture, whereas the UIT sample shows a river pattern with dimples and tearing ridges, wherein the cleavage steps and secondary cracks are not obvious.

(4) Compared with the UWJ sample, the samples produced by LBT and UIT exhibits gradient heterostructures on their surfaces and in certain depth of the samples, which promotes a synergistic improvement in strength and toughness, reduces the probability of crack nucleation and initiation, and promotes crack deflection.

CRediT authorship contribution statement
Yong-heng JIANG: Investigation, Formal analysis, Writing – Original draft, Writing – Review & editing; **Xin-lei QIU:** Investigation, Formal analysis, Writing – Original draft; **Zheng-qiang ZHANG:** Conceptualization, Writing – Review & editing; **Zi-heng SONG:** Validation, Data curation; **Sheng-guang DAI:** Investigation; **Xue-lei WANG:** Investigation; **Chun WU:** Supervision, Resources; **Chao MENG:** Funding acquisition, Resources, Supervision, Validation, Writing – Original draft.

Declaration of competing interest
The authors declare that they have no known competing financial interests or personal relationships that could have appeared to influence the work reported in this paper.

References

[1] YANG Liu, DUAN Yong-chuan, GUAN Ying-ping. Ductile fracture prediction of ZK61M high-strength magnesium alloy sheet during hot deformation process [J]. Transactions of Nonferrous Metals Society of China, 2023, 33(1): 95−106. https://doi.org/10.1016/S1003-6326(22)66093-X.

[2] LI Min-hao, LU Li-wei, FAN Yu-tian, MA Min, WU Zhi-qiang, ZHOU Tao, QI Fu-gang, ZHANG Hua. Microstructure evolution and deformation behavior of AZ31 Mg alloy sheets processed by repeated bending−flattening deformation with different die angles [J]. Transactions of Nonferrous Metals Society of China, 2024, 34(3): 812−832. https://doi.org/10.1016/S1003-6326(23)66436-2.

[3] POLLOCK T M. Weight loss with magnesium alloys [J]. Science, 2010, 328(5981): 986−987. https://doi.org/10.1126/science.1182848.

[4] QIN Bo, YIN Fu-cheng, ZENG Cheng-zong, XIE Jia-cheng, SHEN Jun. Microstructure and mechanical properties of TIG/A-TIG welded AZ61/ZK60 magnesium alloy joints [J]. Transactions of Nonferrous Metals Society of China, 2019, 29(9): 1864−1872. https://doi.org/10.1016/S1003-6326(19)65094-6.

[5] SONG Gang, DIAO Zhuo, LV Xin-ze, LIU Li-ming. TIG and laser-TIG hybrid filler wire welding of casting and wrought dissimilar magnesium alloy [J]. Journal of Manufacturing Processes, 2018, 34: 204−214. https://doi.org/10.1016/j.jmapro.2018.06.005.

[6] PENG Pai, WANG Wen, JIN Yuan-yuan, LIU Qiang, ZHANG Ting, QIAO Ke, CAI Jun, WANG Kuai-she. Experimental investigation on fatigue crack initiation and propagation mechanism of friction stir lap welded dissimilar joints of magnesium and aluminum alloys [J]. Materials Characterization, 2021, 177: 111176. https://doi.org/10.1016/j.matchar.2021.111176.

[7] WANG B, ZHANG P, DUAN Q Q, ZHANG Z J, YANG H J, PANG J C, TIAN Y Z, LI X W, ZHANG Z F. Synchronously improved fatigue strength and fatigue crack growth resistance in twinning-induced plasticity steels [J]. Materials Science and Engineering A, 2018, 711: 533−542. https://doi.org/10.1016/j.msea.2017.11.074.

[8] YU Jiang-ping, ZHANG Xi-yan, SHU Yang, TAN Li, YIN Rui-sen. Evolution characteristics of microstructure and properties in AZ31 alloy during high cycle fatigue processes [J]. Transactions of Nonferrous Metals Society of China, 2017, 27(7): 1530−1536. https://doi.org/10.1016/S1003-6326(17)60173-0

[9] MA Peng-hui, QIAN Li-he, MENG Jiang-ying, LIU Shuai, ZHANG Fu-cheng. Influence of Al on the fatigue crack

growth behavior of Fe−22Mn−(3Al)−0.6C TWIP steels [J]. Materials Science and Engineering A, 2015, 645: 136. https://doi.org/10.1016/j.msea.2015.08.017. 41.

[10] FU Hui, YUAN Shu-qing, CHAN K C, YANG Xu-sheng. Superior strength-ductility synergy and fatigue resistance of heterogeneous structured AZ41 Mg alloy by laser surface processing [J]. Materials Science and Engineering A, 2022, 858: 144151. https://doi.org/10.1016/j.msea.2022.144151.

[11] WU Lu-shen, WANG Teng, HU Yun, LIU Jia-ming, SONG Min-jie. A method for improving the crack resistance of aluminum alloy aircraft skin inspired by plant leaf [J]. Theoretical and Applied Fracture Mechanics, 2020, 106: 102444. https://doi.org/10.1016/j.tafmec.2019.102444.

[12] WANG Chuan-wei, ZHOU Hong, ZHANG Zhi-hui, ZHAO Yu, CONG Da-long, MENG Chao, ZHANG Peng, REN Lu-quan. Mechanical property of a low carbon steel with biomimetic units in different shapes [J]. Optics & Laser Technology, 2013, 47: 114−120. https://doi.org/10.1016/j.optlastec.2012.07.037.

[13] SHI Hai-fang, ZHANG Zheng-qiang, SUI Qi, WANG Xue-lei, REN Xin, WU Chun, ZHUANG Wei-bin, MENG Chao. Study of fatigue crack growth characteristics of TIG welded AZ31B magnesium alloy joint based on laser bionic treatment [J]. Fatigue & Fracture of Engineering Materials & Structures, 2022, 45(11): 3167−3182. https://doi.org/10.1111/ffe.13806.

[14] CASTILLO-MORALES M, BERBER-SOLANO T P, SALAS-ZAMARRIPA A, ZAPATA-HERNÁNDEZ O J, HERNÁNDEZ-SANDOVAL J, LEDEZMA-RAMÍREZ D F, CASTILLO-ELIZONDO J A, ALDACO-CASTAÑEDA J A. Effectiveness of the ultrasonic impact treatment in the retardation of the fatigue crack growth for 2024-T3 Al alloy components [J]. The International Journal of Advanced Manufacturing Technology, 2020, 108: 157−165. https://doi.org/10.1007/s00170-020-05064-9.

[15] DEKHTYAR A I, MORDYUK B N, SAVVAKIN D G, BONDARCHUK V I, MOISEEVA I V, KHRIPTA N I. Enhanced fatigue behavior of powder metallurgy Ti−6Al−4V alloy by applying ultrasonic impact treatment [J]. Materials Science and Engineering A, 2015, 641: 348−359. https://doi.org/10.1016/j.msea.2015.06.072.

[16] CHEN Wen-jing, HUANG Chun-ping, LIU Feng-gang, LIANG Ren-yu, LIU Fen-cheng, YANG Hai-ou. Microstructure and properties of Ti60 alloy by laser solid forming and ultrasonic impact hybrid manufacturing [J]. Transactions of Nonferrous Metals Society of China, 2023, 33(11): 3319−3331. https://doi.org/10.1016/S1003-6326(23)66336-8.

[17] CHEN Fu-rong, YANG Yi-hang, LI Nan. Effect of ultrasonic impact time on microstructure and properties of 7A52 aluminum alloy tandem MIG welded joint [J]. The International Journal of Advanced Manufacturing Technology, 2021, 116: 2687−96. https://doi.org/10.1007/s00170-021-07599-x.

[18] PADMANABAN G, BALASUBRAMANIAN V, REDDY G M. Fatigue crack growth behaviour of pulsed current gas tungsten arc, friction stir and laser beam welded AZ31B magnesium alloy joints [J]. Journal of Materials Processing Technology, 2011, 211(7): 1224−1233. https://doi.org/10.

1016/j.jmatprotec.2011.02.003.

[19] LIU Zhe, GUO Xiang-yu, CUI Hai-chao, LI Fang, LU Feng-gui. Role of misorientation in fatigue crack growth behavior for NG-TIG welded joint of Ni-based alloy [J]. Materials Science and Engineering A, 2018, 710: 151−163. https://doi.org/10.1016/j.msea.2017.10.090.

[20] CULBERTSON D, JIANG Yan-yao. An experimental study of the orientation effect on fatigue crack propagation in rolled AZ31B magnesium alloy [J]. Materials Science and Engineering A, 2016, 676: 10−19. https://doi.org/10.1016/j.msea.2016.08.088.

[21] ZHENG San-long, YU Qin, JIANG Yan-yao. An experimental study of fatigue crack propagation in extruded AZ31B magnesium alloy [J]. International Journal of Fatigue, 2013, 47: 174−183. https://doi.org/10.1016/j.ijfatigue.2012.08.010.

[22] ZHENG San-long, YU Qin, GAO Zeng-liang, JIANG Yan-yao. Loading history effect on fatigue crack growth of extruded AZ31B magnesium alloy [J]. Engineering Fracture Mechanics, 2013, 114: 42−54. https://doi.org/10.1016/j.engfracmech.2013.10.012.

[23] UEMATSU Y, KAKIUCHI T, NAKAJIMA M, NAKAMURA Y, MIYAZAKI S, MAKINO H. Fatigue crack propagation of AZ61 magnesium alloy under controlled humidity and visualization of hydrogen diffusion along the crack wake[J]. International Journal of Fatigue, 2014, 59: 234−243. https://doi.org/10.1016/j.ijfatigue.2013.08.014.

[24] ZHANG Hong-xia, YAN Zhi-feng, WANG Wen-xian, LIANG Pei-yang, LI Hong-zhi, WEI Ying-hui. As-extruded AZ31B magnesium alloy fatigue crack propagation behavior [J]. Journal of Wuhan University of Technology (Mater Sci Ed), 2011, 26: 1114−1120. https://doi.org/10.1007/s11595-011-0373-3.

[25] LI Lin, YANG Jie, YANG Zhi-yuan, SUN Qi, TAN Li, ZENG Qing-hui, ZHU Min-hao. Towards revealing the relationship between deformation twin and fatigue crack initiation in a rolled magnesium alloy [J]. Materials Characterization, 2021, 179: 111362. https://doi.org/10.1016/j.matchar.2021.111362.

[26] PRIBE J D, SIEGMUND T, KRUZIC J J. The roles of yield strength mismatch, interface strength, and plastic strain gradients in fatigue crack growth across interfaces [J]. Engineering Fracture Mechanics, 2020, 235: 107072. https://doi.org/10.1016/j.engfracmech.2020.107072.

[27] YU Da-liang, ZHANG Ding-fei, DAI Qing-wei, LAN Wei, PENG Jian, XU Jun-yao, QI Fu-gang, PAN Fu-sheng. Effect of stress ratio on high cycle fatigue properties in Mg−6Zn−1Mn alloy [J]. Materials Science and Engineering A, 2018, 711: 624−632. https://doi.org/10.1016/j.msea.2017.10.082.

[28] PANDEY V, CHATTOPADHYAY K, SRINIVAS N C S, SINGH V. Role of ultrasonic shot peening on low cycle fatigue behavior of 7075 aluminium alloy [J]. International Journal of Fatigue, 2017, 103: 426−435. https://doi.org/10.1016/j.ijfatigue.2017.06.033.

[29] GE Mao-zhong, XIANG Jian-yun. Effect of laser shock peening on microstructure and fatigue crack growth rate of AZ31B magnesium alloy [J]. Journal of Alloys and Compounds, 2016, 680: 544−552. https://doi.org/10.1016/j.

jallcom.2016.04.179.

[30] SHEN Jia-jia, LOPES J G, ZENG Z, CHOI Y T, MAAWAD E, SCHELL N, KIM H S, MISHRA R S, OLIVEIRA J P. Deformation behavior and strengthening effects of an eutectic AlCoCrFeNi2.1 high entropy alloy probed by in-situ synchrotron X-ray diffraction and post-mortem EBSD [J]. Materials Science and Engineering A, 2023, 872: 144946. https://doi.org/10.1016/j.msea.2023.144946.

[31] WANG Ping, YE Ling-ying, LIU Xiao-dong, DONG Yu, ZHAO Li. Effects of grain structures on fatigue crack propagation behavior of an Al−Cu−Li alloy [J]. International Journal of Fatigue, 2023, 177: 107927. https://doi.org/10.1016/j.ijfatigue.2023.107927.

[32] ZHU Yun-tian, WU Xiao-lei. Perspective on hetero-deformation induced (HDI) hardening and back stress [J]. Materials Research Letters, 2019, 7: 393−398. https://doi.org/10.1080/ 21663831.2019.1616331.

[33] LIN P T, LIU H C, HSIEH P Y, WEI C Y, TSAI C W, SATO Y S, CHEN S C, YEN H W, LU N H, CHEN C H. Heterogeneous structure-induced strength−ductility synergy by partial recrystallization during friction stir welding of a high-entropy alloy [J]. Materials & Design, 2021, 197: 109238. https://doi.org/10.1016/j.matdes.2020.109238.

[34] YANG Mu-xin, PAN Yue, YUAN Fu-ping, ZHU Yun-tian, WU Xiao-lei. Back stress strengthening and strain hardening in gradient structure [J]. Materials Research Letters, 2016, 4: 145−151. https://doi.org/ 10.1080/21663831.2016.1153004.

[35] ZHU Yun-tian, AMEYAMA K, ANDERSON P M, BEYERLEIN I J, GAO Hua-jian, KIM H S, LAVERNIA E, MATHAUDHU S, MUGHRABI H, RITCHIE R O, TSUJI N, ZHANG Xiang-yi, WU Xiao-lei. Heterostructured materials: superior properties from hetero-zone interaction [J]. Materials Research Letters, 2021, 9: 1−31. https://doi.org/10.1080/21663831.2020.1796836.

[36] MENG Chao, JIANG Yong-heng, YANG Jun-tao, ZHANG Zheng-qiang, QIU Xin-lei, WU Chun, LI Ming-sheng, REN Xin. The effect of combined laser bionic and ultrasonic impact on the microstructure and fatigue properties of AZ31B magnesium alloy TIG welded joints [J]. International Journal of Fatigue, 2023, 176: 107881. https://doi.org/10.1016/j.ijfatigue.2023.107881.

[37] CHEN Fu-rong, LIU Cheng-hao. Improving the properties of laser-welded Al−Zn−Mg−Cu alloy joints by aging and double-sided ultrasonic impact compound treatment [J]. Materials, 2021, 14(11): 2742. https://doi.org/10.3390/ma14112742

[38] LV You, LEI Li-qun, SUN Li-na. Influence of different combined severe shot peening and laser surface melting treatments on the fatigue performance of 20CrMnTi steel gear [J]. Materials Science and Engineering A, 2016, 658: 77−85. https://doi.org/10.1016/j.msea.2016.01.050.

[39] CAI Xiao-jing, XIA Ri, HUO Ming-chen, XU Jin-quan. A threshold formula for fatigue crack growth with mean stress intensity factors [J]. International Journal of Mechanical Sciences, 2018, 135: 639−645. https://doi.org/10.1016/j.ijmecsci.2017.12.014.

不同仿生强化技术对 AZ31B 镁合金 TIG 焊接接头疲劳裂纹扩展行为的影响

姜永恒 [1]，邱心雷 [1]，张正强 [1]，宋子衡 [2]，戴胜广 [1]，王学雷 [1]，吴 纯 [1]，孟 超 [1]

1. 辽宁工程技术大学 材料科学与工程学院，阜新 123000；
2. 东北大学 材料电磁过程研究教育部重点实验室，沈阳 110819

摘 要：为了提高镁合金焊接接头在循环载荷下的疲劳性能，研究并对比分析了激光仿生处理和超声冲击仿生处理对 AZ31B 镁合金 TIG 焊接接头疲劳裂纹扩展(FCG)行为的影响。结果表明，仿生处理细化接头表面的晶粒，提高显微硬度。在裂纹稳定扩展阶段，两种仿生试样均表现出较低的 FCG 速率和较高的 FCG 抗性。两种仿生处理方法均降低裂纹萌生的概率，一定程度上促进裂纹偏转，为改善焊接接头 FCG 行为提供新的途径。

关键词：镁合金；激光仿生处理；超声冲击仿生处理；显微组织；疲劳裂纹扩展

(Edited by Bing YANG)